LATENT PDE MAPPING FOR SHAPE-GENERALIZABLE PHYSICS-INFORMED NEURAL NETWORKS

Anonymous authors

 Paper under double-blind review

ABSTRACT

Physics-Informed Neural Networks (PINNs) have shown strong potential for learning physically consistent representations from sparse data, but often struggle to generalize to geometries with varying shapes. To address this challenge, we introduce *latent PDE mapping*, a technique for mapping geometry-specific partial differential equations (PDEs) to a shared latent PDE representation using the deformation gradient. We embed latent PDE mapping into the PINN framework (LPM-PINN), enabling PINNs to capture geometric variability while preserving the governing physics. This integration facilitates accurate predictions of nonlinear, time-dependent systems even in geometries well beyond the training distribution. We demonstrate LPM-PINN on a challenging nonlinear time-dependent PDE with sharp gradients, the Aliev–Panfilov model of cardiac electrophysiology, in both 2D and 3D. Our results show that LPM-PINN generalizes robustly across diverse geometries, including shapes with drastically changing boundaries. These findings establish latent PDE mapping as a promising approach for extending PINNs to applications with variable geometries and complex physics.

1 Introduction

Physics-informed neural networks (PINNs) (Raissi et al., 2019) have emerged as a new paradigm for learning physically consistent representations from sparse observations (Karniadakis et al., 2021; Cuomo et al., 2022). However, PINNs face significant challenges when making predictions on geometries with varying shapes, often requiring retraining when encountering novel morphologies outside the training distribution (Gao et al., 2021). This limitation is critical in time-sensitive applications (e.g. medicine) where short compute times and generalization across diverse physiologically-derived shapes are required. Here, we have chosen a prominent example that arises in cardiac electrophysiology, where accurate cardiac arrest risk assessments require adaptation to diverse heart geometries, and integration into medical workflows requires fast computations.

To address this issue, we introduce *latent PDE mapping*, a technique that maps geometry-specific partial differential equations (PDEs) to a shared latent PDE representation. Using affine shape parameterization, a predefined latent geometry, and the deformation gradient; our method expresses the loss terms of a PINN (LPM-PINN) using latent coordinates. This approach preserves the underlying dynamics while capturing geometric variability, enabling accurate predictions on unseen shapes in nonlinear, time-dependent systems. We apply latent PDE mapping to the Aliev-Panfilov model of cardiac electrophysiology, a representative benchmark for challenging nonlinear time-dependent PDE dynamics. The proposed approach offers a broadly applicable strategy for extending PINNs to problems involving geometries with variable shapes.

1.1 OUR CONTRIBUTIONS

- We introduce *latent PDE mapping*, a novel technique that maps geometry-specific PDEs to a shared latent PDE, enabling PINNs to learn meaningful representations from sparse observations across diverse geometrical shapes.
- We construct a PINN (LPM-PINN), which applies latent PDE mapping to the Aliev-Panfilov model of cardiac electrophysiology, a challenging nonlinear, time-

dependent PDE with sharp gradients in 2D and 3D. LPM-PINN provides accurate solutions even in extreme rotation scenarios where the boundary changes radically.

 We provide theoretical and empirical evidence that latent PDE mapping properly accounts for geometric variability in the physics loss gradient, yielding more generalizable representations.

2 RELATED WORK

Several approaches have explored extensions of PINNs to variable geometries. The earliest studies modified network architectures, replacing multilayer perceptrons with physics-informed convolutional neural networks (Gao et al., 2021), physics-informed graph neural networks (Dalton et al., 2023; Peng et al., 2023; Würth et al., 2024; Gao et al., 2022), or physics-informed PointNet (Kashefi & Mukerji, 2022). These models are better suited to handle variable geometries than basic PINNs, but require uniform grids, complex meshing at inference, or struggle to generalize across PDE parameters (Zhong & Meidani, 2025). To overcome these challenges, other studies have instead augmented PINNs with shape descriptors (Regazzoni et al., 2022; Costabal et al., 2024) or global geometric parameters (Sun et al., 2023; Ghosh et al., 2024). While showing promising results, these methods still couple the learning process to specific shapes, which can result in suboptimal training and limited generalization.

Another research direction involves latent geometries, where inputs are embedded into a common latent space to facilitate comparison and efficient representation across different shapes. Regazzoni et al. (2022) proposed a universal latent space for parameterized geometries, enabling learning across varying shapes. Similarly, Mezzadri et al. (2023) introduced a framework that aligns geometric variability through latent embeddings, enabling simple linear elasticity models to generalize across freeform domains. More recently, Burbulla (2023) introduced a PDE mapping to low-dimensional manifolds and applied it to simple linear PDEs. However, all previously mentioned latent geometry studies are limited to simple, linear, static PDEs. This limits the methods' utility in real-world applications, which are often complex, nonlinear, and dynamic. Moreover, no work has yet shown that PINNs with mapped PDEs can generalize well to diverse geometries.

The latent PDE mapping introduced here moves beyond simple PDE mapping to PINN formulations with geometrically variable shapes and nonlinear, time-dependent PDEs. Furthermore, we introduce the use of the deformation gradient to accurately map nonlinear PDEs within PINNs.

3 LATENT PDE MAPPING

We consider a time-dependent PDE defined over a geometry $\Omega(s)$. Here, s is a set of shape parameters describing the overall geometry of Ω . The governing PDE is given as

$$\mathcal{F}(u(\boldsymbol{x},t;s)) = f(\boldsymbol{x},t,u;s), \qquad (\boldsymbol{x},t) \in \Omega(s) \times \mathcal{T}$$
(1)

where $\mathcal F$ denotes a differential operator, f represents a source term that introduces external influences into the system, $\boldsymbol x\in\Omega(s)\subset\mathbb R^d$ are the spatial coordinates, $t\in\mathcal T\subset\mathbb R$ is the time, and u is the unknown PDE solution. In practice, obtaining an exact solution to equation 1 is often intractable due to the complexity of the underlying system. To address this, we employ a PINN to approximate the solution such that

$$\mathcal{N}\mathcal{N}(\boldsymbol{x},t,s;\theta) = u_{\theta} \approx u(\boldsymbol{x},t;s)$$
 (2)

where θ represents the trainable parameters. PINNs are known to offer a data-efficient machine learning alternative by embedding physical laws directly into the neural network via PDE residuals in the loss function (Raissi et al., 2019). The residual is defined as

$$\mathcal{R} = \mathcal{F}(u(\boldsymbol{x}, t; s)) - f(\boldsymbol{x}, t, u; s) = 0, \qquad (\boldsymbol{x}, t) \in \Omega(s) \times \mathcal{T}$$
(3)

where \mathcal{R} depends on $\Omega(s)$ and the shape parameters s. With latent PDE mapping, we rather express the geometry-specific residual in equation 3 over a latent geometry. Thus, we assume that there exists a continuous map between $\Omega(s)$ and a predefined latent geometry Ω_0 , defined as

$$\Phi := X \to x \tag{4}$$

where X is a given point in Ω_0 while x is the associated point in $\Omega(s)$. Physical quantities can be mapped from $\Omega(s)$ to Ω_0 , or vice versa, through the deformation gradient and deformation Jacobian given as

$$\mathbf{F}(\boldsymbol{X},t,s) = \mathbf{I} + \nabla U(\boldsymbol{X},t,s) \tag{5}$$

and $J(\boldsymbol{X},t,s) = \det(\boldsymbol{F})$, respectively (Holzaphel, 2000). Here, \boldsymbol{I} is the identity tensor and $U(\boldsymbol{X},t,s) = \boldsymbol{x}(\boldsymbol{X},t,s) - \boldsymbol{X}$ is the displacement field at time t for the shape parameters s. In this study, we use the deformation gradient to map the geometry-specific \mathcal{R} in equation 3 to a shared latent representation, yielding

$$\mathcal{R}(\boldsymbol{X}, t, u, \boldsymbol{\mathsf{F}}, J) = \mathcal{F}(u(\boldsymbol{X}, t; s), \boldsymbol{\mathsf{F}}, J) - f(\boldsymbol{X}, t, u, \boldsymbol{\mathsf{F}}, J; s), \qquad (\boldsymbol{X}, t) \in \Omega_0 \times \mathcal{T}. \tag{6}$$

In this way, the dependency on s has been moved from the physical geometry $\Omega(s)$ into the PDE itself through the deformation gradient \mathbf{F} . This approach is what we refer to as the *latent PDE mapping* technique.

3.1 APPLICATION TO NONLINEAR, TIME-DEPENDENT, STIFF SYSTEMS: THE ALIEV-PANFILOV PDE

We demonstrate our latent PDE mapping technique on the Aliev-Panfilov model from cardiac eletrophysiology. The Aliev-Panfilov PDE (Aliev & Panfilov, 1996) is used to describe the evolution of transmembrane potential V over a physical geometry representing cardiac tissue and offers a fair representation of challenging PDEs due to its nonlinearity, sharp gradients, and time-dependency. The PDE can be expressed over a physical geometry $\Omega(s)$ as

$$\begin{cases} \frac{\partial V}{\partial \tau} = \nabla \cdot (\mathbf{D}\nabla V) - kV(V - a)(V - 1) - VW & \text{in } \Omega(s), \\ \frac{\partial W}{\partial \tau} = \left(\epsilon_0 + \frac{\mu_1 W}{V + \mu_2}\right) \left(-W - kV\left(V - a - 1\right)\right) & \text{in } \Omega(s), \\ \mathbf{D}\nabla V \cdot \boldsymbol{n} = 0 & \text{on } \partial \Omega(s) \end{cases}$$
(7)

where V,W, and τ are dimensionless variables representing the transmembrane potential, recovery variable, and time, respectively. $V \in [0,1]$ is given in arbitrary units (AU), while $\tau=12.9t$ is measured in temporal units (TU) with t given in milliseconds. The tissue conductivity is defined by the diffusion tensor \mathbf{D} , while $k,a,\epsilon_0,\mu_1,\mu_2$ are parameters controlling the overall shape and temporal dynamics of V and W. Additionally, the PDE employs a no-flux Neumann boundary condition where n is the vector normal to the boundary of $\Omega(s)$. Consequently, there is no leakage of V to regions outside of $\Omega(s)$.

We apply our latent PDE mapping technique to the Aliev-Panfilov PDE in equation 7. For a time-independent mapping, the latent PDE representation is given as

$$\begin{cases} \frac{\partial V}{\partial \tau} = \frac{1}{J} \nabla \cdot (J \mathbf{F}^{-1} \mathbf{D} \mathbf{F}^{-T} \nabla V) - kV(V - a)(V - 1) - VW & \text{in } \Omega_{0}, \\ \frac{\partial W}{\partial \tau} = \left(\epsilon_{0} + \frac{\mu_{1} W}{V + \mu_{2}}\right) (V, W) \left(-W - kV \left(V - a - 1\right)\right) & \text{in } \Omega_{0}, \\ J \mathbf{F}^{-1} \mathbf{D} \mathbf{F}^{-T} \nabla V \cdot \mathbf{N} = 0 & \text{on } \partial \Omega_{0}, \end{cases}$$
(8)

where N is the normal vector to the boundary of the latent geometry Ω_0 , $\mathbf{F} = \mathbf{F}(\mathbf{X}, t, s)$ and $J = J(\mathbf{X}, t, s)$. A detailed derivation of equation 8 can be found in Appendix A.

3.2 ACCURATE GRADIENT CALCULATION WITH LATENT PDE MAPPING

The physics loss in PINNs is typically evaluated with the mean squared error (MSE) of \mathcal{R} (Wang et al., 2023), given as

$$\mathcal{L}_{phys} = \frac{1}{N_{phys}} \sum_{i}^{N_{phys}} \mathcal{R}_i^2 \tag{9}$$

using a traditional mini-batch approach with N_{phys} collocation points to evaluate \mathcal{R} . This approach treats \mathcal{R} as independent of $\Omega(s)$ during optimization, which is not the case and can lead to inaccurate gradient estimates. Thus, a more accurate formulation is to evaluate the physics loss as a continuous integral

$$\mathcal{L}_{phys} = \int_{\Omega(s)} \mathcal{R}(\boldsymbol{x}, t, u, s)^2 d\Omega$$
 (10)

and apply the Leibniz integral rule when computing the shape gradient $\frac{\partial \mathcal{L}_{phys}}{\partial s}$. This results in

$$\frac{\partial \mathcal{L}_{phys}}{\partial s} = \int_{\Omega(s)} \frac{\partial}{\partial s} \mathcal{R}(\boldsymbol{x}, t, u, s)^2 d\Omega + \int_{\partial \Omega(s)} \mathcal{R}(\boldsymbol{x}, t, u, s)^2 \frac{\partial \boldsymbol{x}}{\partial s} \cdot \boldsymbol{n} dS$$
(11)

where n is the outward unit normal to the boundary $\partial\Omega(s)$ and $\mathrm{d}S$ is an infinitesimally small part of the boundary. The second term in equation 11 accounts for the movement of the boundary, which is neglected in the discrete loss formulation in equation 9. This omission can lead to inaccurate gradient estimates, hindering training and resulting in suboptimal PINNs.

With latent PDE mapping, the dependency of s is moved from the geometry into the PDE itself via the deformation gradient \mathbf{F} . Consequently, the integrand does not vary with s and the shape gradient can be computed directly

$$\frac{\partial \mathcal{L}_{phys}}{\partial s} = \int_{\Omega_0} \frac{\partial}{\partial s} \mathcal{R}(\boldsymbol{X}, t, u, \boldsymbol{\mathsf{F}}, J)^2 d\Omega_0. \tag{12}$$

Thus, the straightforward MSE in equation 9 can be applied during training without sacrificing gradient accuracy. Based on these considerations, we hypothesized that improving the accuracy of the physics loss gradient via latent PDE mapping can improve the generalizability of PINNs to novel geometries.

4 CARDIAC ELECTROPHYSIOLOGY DATASETS WITH VARIABLE GEOMETRIES

We constructed four and seven families of geometries in 2D and 3D, respectively, for training and testing of our PINNs. In 2D, the latent geometry Ω_0 was defined as a 10×10 mm square, while in 3D it was a $10\times 10\times 10$ mm cube. Families belonging to 2D and 3D are denoted with a $\mathcal G$ and $\mathcal H$, respectively. In the following, we describe the generation of 2D datasets. The extension to 3D is straightforward and provided in detail in Appendix B.2.

The geometries were generated by deforming Ω_0 through different affine transformations expressed in their most general form as

$$x = AX + X^T M X \tag{13}$$

with

$$\mathbf{A} = \begin{bmatrix} a_1 & a_2 \\ a_3 & a_4 \end{bmatrix}, \qquad \mathbf{M} = \begin{bmatrix} m_1 & 0 \\ 0 & m_4 \end{bmatrix}. \tag{14}$$

The elements of A and M, referred to as *affine parameters*, are denoted by $s = \{a_1, a_2, a_3, a_4, m_1, m_4\}$. Each family of geometries corresponded to a distinct deformation type: expansion (\mathcal{G}_{exp}) , shearing (\mathcal{G}_{shear}) , nonlinear deformation (\mathcal{G}_{nonlin}) , and rotation (\mathcal{G}_{rot}) . Figure 1 illustrates one representative geometry from each family, while Table 4 in Appendix B.1 gives the affine parameter ranges for all families.

For each family, we generated two branches. The first branch (\mathcal{G}_k) contained 50 geometries, which were later split into training, validation, and test sets. The second branch (\mathcal{G}_k^*) contained 35 geometries generated from parameter ranges outside those of \mathcal{G}_k , and was used exclusively for testing. We refer to test geometries in \mathcal{G}_k as the *internal family* and \mathcal{G}_k^* as the *external family*.

In 3D, the same procedure was applied with the same number of geometries and versions per family. However, only linear deformation types were considered. The 3D families are denoted as \mathcal{H}_k^p where k indicates the deformation type (expansion, shearing, or rotation) and p indicates the direction of the deformation when applicable (\mathcal{H}_{rot}^x = rotation about the x-axis, \mathcal{H}_{shear}^{xy} = shearing along the xy-plane, etc.).

Synthetic cardiac electrophysiology data We used *openCARP* (Plank* et al., 2021; openCARP consortium et al., 2024) to create synthetic data that was used to approximate the ground truth PDE solution during training and testing of the PINNs. Thus, we solved the Aliev-Panfilov PDE in equation 7 over the physical geometries using the finite element method (FEM). All geometries were stimulated by an external current at nodes located at the left boundary/plane. Sheet fibers were oriented along the x-axis with isotropic conductivities, resulting in a planar wave propagation. All

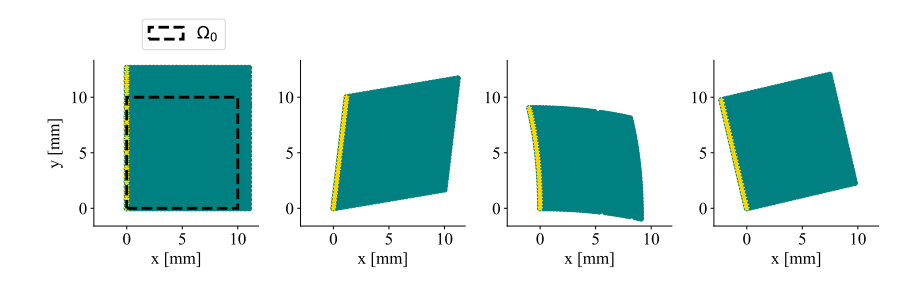


Figure 1: From left to right, the figure shows an example of a geometry from \mathcal{G}_{exp} , \mathcal{G}_{shear} , \mathcal{G}_{nonlin} , and \mathcal{G}_{rot} . All geometries were externally stimulated at the left edge nodes (yellow). The dashed line illustrates the latent geometry Ω_0 in 2D.

simulations were run for $520 \, \mathrm{ms}$, yielding a full cycle of polarization and re-polarization. Solutions at $t < 6 \, \mathrm{ms}$ were excluded to remove applied current from the system. The exact configurations used for synthetic data generation are listed in Table 7 in Appendix D.

5 PINN TRAINING PROCEDURES AND EVALUATION METHODS

We developed three PINNs for comparison and evaluation of the latent PDE mapping. The first PINN (LPM-PINN) incorporates the latent PDE mapping technique and uses affine parameters as additional inputs. The second (Affine-PINN) and third (Basic-PINN) PINNs adopt the conventional physics loss formulated over the physical geometries. However, the Affine-PINN integrates affine parameters as input, whereas the Basic-PINN relies exclusively on spatiotemporal inputs. This setup enables a systematic evaluation of the contribution of latent PDE mapping to PINN training, as well as the added benefits of including affine parameters.

All PINNs were trained by minimizing a hybrid loss function defined as

$$\mathcal{L}(\theta) = \mathcal{L}_{data}(\theta) + \mathcal{L}_{phys}(\theta) + \mathcal{L}_{bc}(\theta) + \mathcal{L}_{ic}(\theta)$$
(15)

where $\mathcal{L}_{data}(\theta)$ is the loss due to known FEM data, $\mathcal{L}_{phys}(\theta)$ is the loss described by the governing PDE residual, $\mathcal{L}_{bc}(\theta)$ is the loss associated with the boundary condition, and $\mathcal{L}_{ic}(\theta)$ is the loss associated with the initial condition. The loss terms were equally weighted, and each term was evaluated using the MSE over a given set of spatiotemporal points $(\mathcal{N}_{data}, \mathcal{N}_{phys}, \mathcal{N}_{bc}, \mathcal{N}_{ic})$. Furthermore, we defined the physics and boundary loss in LPM-PINN as

$$\mathcal{L}_{phys}^{LPM} \equiv \frac{1}{\mathcal{N}_{phys}} \sum_{s}^{\mathcal{N}_{phys}} \mathcal{R}(\boldsymbol{X}, \tau, \hat{V}, \hat{W}, \boldsymbol{\mathsf{F}}, J), \qquad \mathcal{L}_{bc}^{LPM} \equiv \frac{1}{\mathcal{N}_{bc}} \sum_{s}^{\mathcal{N}_{bc}} \mathcal{R}(\boldsymbol{X}, \tau, \hat{V}, \boldsymbol{\mathsf{F}}, J) \quad (16)$$

and the conventional losses in Affine-PINN and Basic-PINN as

$$\mathcal{L}_{phys}^{conv} \equiv \frac{1}{\mathcal{N}_{phys}} \sum_{k}^{\mathcal{N}_{phys}} \mathcal{R}(\boldsymbol{x}, \tau, \hat{V}, \hat{W}), \qquad \mathcal{L}_{bc}^{conv} \equiv \frac{1}{\mathcal{N}_{bc}} \sum_{k}^{\mathcal{N}_{bc}} \mathcal{R}(\boldsymbol{x}, \tau, \hat{V}).$$
(17)

where $X \in \Omega_0$ and $x \in \Omega(s)$. We used a fully connected neural network with 10 hidden layers in each PINN. Each layer had 25 neurons, and we employed the tanh as activation function to handle second-order derivatives in the backward pass. All PINNs predicted \hat{V} and \hat{W} as outputs. A complete overview of the hyperparameters for each PINN can be found in Table 6 in Appendix C.

Each internal family $(\mathcal{G}_k, \mathcal{H}_k)$ was split into a training set, validation set, and test set. Unlike the conventional split used in machine learning, we adopted an inverted allocation strategy with 20% train data (10 geometries), 10% validation data (5 geometries), and 70% test data (35 geometries) in order to emphasize the applicability of PINNs in data-limited regimes. Furthermore, we selected $\mathcal{N}_{data}=14, \mathcal{N}_{phys}=700, \mathcal{N}_{bc}=80$, and $\mathcal{N}_{ic}=30$ spatial locations from each geometry in the training set and trained the models for 5000 epochs. $\mathcal{N}_{phys}, \mathcal{N}_{bc}$, and \mathcal{N}_{ic} were resampled at every epoch to ensure that the physics was learned over the entire geometry.

During training, we evaluated $\mathcal{L}(\theta)$ for each geometry in the validation set. Since our validation set spanned multiple distinct geometries, we selected the best PINN state as the state that gave the

lowest maximum $\mathcal{L}(\theta)$ across the validation geometries, rather than the lowest average $\mathcal{L}(\theta)$. This criterion ensured that the PINN generalized effectively to geometries differing substantially from those seen during training. To reduce computational overhead, we computed the validation loss every 10 epochs using a subsample of points from each geometry.

Evaluation metrics We employed the relative L_2 error (ε_{L2}) as an evaluation metric, given as

$$\varepsilon_{L2} = \frac{\sqrt{\sum_{i}^{N_{test}} \left(\hat{V}_{i} - V_{i}\right)^{2}}}{\sqrt{\sum_{i}^{N_{test}} V_{i}^{2}}}$$
(18)

where \hat{V} is the predicted transmembrane potential and V is the approximated FEM data used as ground truth. Results are presented as the mean relative L_2 error across all geometries in the given family with the corresponding standard deviation.

6 EXPERIMENTS

In the following sections, we present results from a series of experiments used to evaluate and compare the PINNs' performance when generalizing across diverse geometries in 2D and 3D. Furthermore, we investigate the role of the missing boundary shape gradients when latent PDE mapping is not applied.

6.1 Does latent PDE mapping improve geometric generalizability in 2D?

The results indicate consistently low prediction errors for all PINNs across test geometries in the internal families \mathcal{G}_{exp} , \mathcal{G}_{shear} , and \mathcal{G}_{nonlin} (Table 1). Moreover, the results show that LPM-PINN and Affine-PINN generalize to the corresponding external families with only a modest increase in prediction error, whereas the Basic-PINN exhibits errors of an order of magnitude higher on the same families. Notably, LPM-PINN is the only PINN that achieves accurate predictions on the \mathcal{G}_{rot}^* family, while Affine-PINN and Basic-PINN yield significantly inaccurate results, as illustrated in the last row of Figure 2. These findings demonstrate that latent PDE mapping improves geometric generalizability, particularly when the boundary undergoes radical changes.

Table 2 shows that LPM-PINN can learn and make accurate predictions when trained on geometries from two different families. In contrast, Affine-PINN and Basic-PINN fail to learn meaningful representations in the same setting, except for Affine-PINN on $\mathcal{G}_{shear}+\mathcal{G}_{rot}$. Figure 5 in Appendix E.1 visualizes predictions on the same geometries as in Figure 2, showing that the higher error is not limited to the \mathcal{G}_{rot} and \mathcal{G}_{rot}^* family, but arises from degraded performance across both families. Hence, the results indicate that latent PDE mapping can enhance generalizability when learning across fundamentally different geometries.

Table 1: Mean relative L_2 PINN-FEM discrepancy \pm std evaluated over the internal (\mathcal{G}_k) and external (\mathcal{G}_k^*) test geometries of each geometry family in 2D.

	LPM-PINN	Affine-PINN	Basic-PINN
$\overline{\mathcal{G}_{exp}}$	0.019 ± 0.004	0.024 ± 0.005	0.057 ± 0.028
\mathcal{G}_{exp}^*	$\textbf{0.044} \pm \textbf{0.013}$	0.070 ± 0.036	0.166 ± 0.043
\mathcal{G}_{shear}	0.024 ± 0.002	0.029 ± 0.004	0.082 ± 0.029
\mathcal{G}^*_{shear}	$\textbf{0.074} \pm \textbf{0.027}$	0.077 ± 0.024	0.203 ± 0.041
\mathcal{G}_{nonlin}	0.029 ± 0.005	0.029 ± 0.009	0.058 ± 0.024
\mathcal{G}^*_{nonlin}	0.055 ± 0.020	$\textbf{0.054} \pm \textbf{0.019}$	0.126 ± 0.044
\mathcal{G}_{rot}	$\textbf{0.017} \pm \textbf{0.001}$	0.055 ± 0.016	0.229 ± 0.021
\mathcal{G}^*_{rot}	$\textbf{0.020} \pm \textbf{0.002}$	0.272 ± 0.137	0.331 ± 0.042

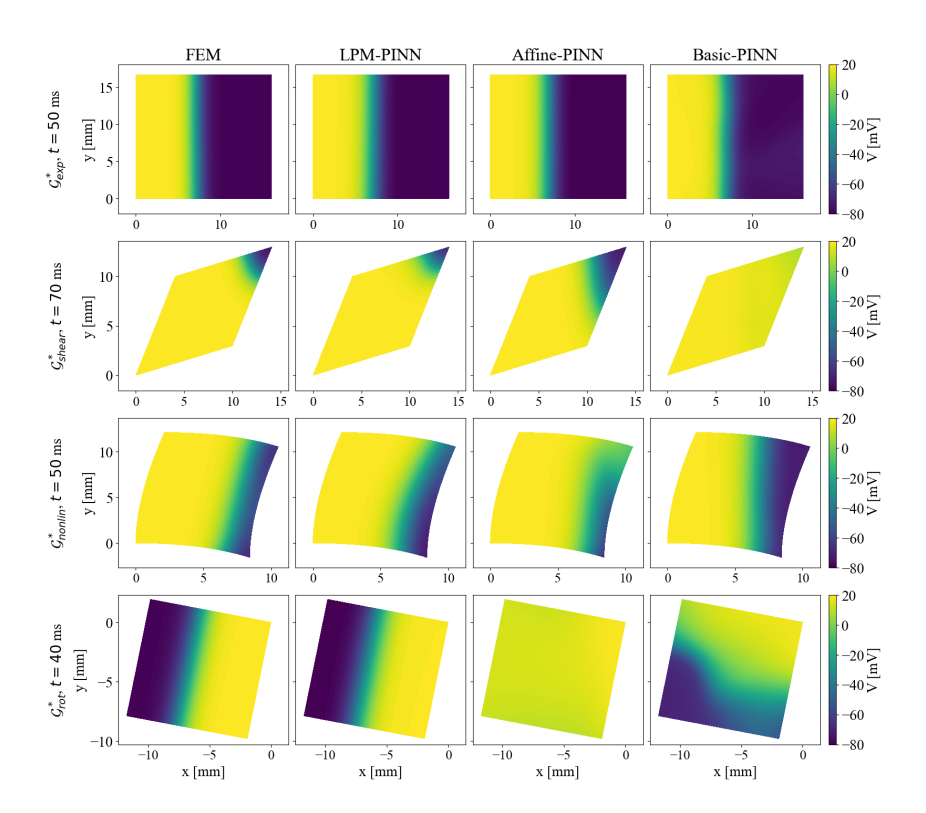


Figure 2: Snapshots of predicted transmembrane voltages (V). Each row corresponds to a geometry taken from the presented external family $(\mathcal{G}^*_{exp}, \mathcal{G}^*_{shear}, \mathcal{G}^*_{nonlin}, \mathcal{G}^*_{rot})$ at a given time point. The left column shows the FEM ground truth approximation.

Table 2: Mean relative L_2 PINN-FEM discrepancy \pm std evaluated over the internal (\mathcal{G}_k) and external (\mathcal{G}_k^*) test geometries from a combination of families in 2D. In this setting, the PINNs were trained on 20 geometries, validated on 10 geometries, and tested on 70 geometries sampled from the corresponding families.

-	LPM-PINN	Affine-PINN	Basic-PINN
\mathcal{G}_{exp} + \mathcal{G}_{rot}	0.022 ± 0.006	0.911 ± 0.065	0.199 ± 0.061
\mathcal{G}_{exp}^* + \mathcal{G}_{rot}^*	$\textbf{0.138} \pm \textbf{0.102}$	1.111 ± 0.268	0.285 ± 0.084
$\mathcal{G}_{shear} + \mathcal{G}_{rot}$	$\textbf{0.021} \pm \textbf{0.005}$	0.027 ± 0.003	2.571 ± 0.067
\mathcal{G}^*_{shear} + \mathcal{G}^*_{rot}	$\textbf{0.048} \pm \textbf{0.033}$	0.152 ± 0.128	2.634 ± 0.174
\mathcal{G}_{nonlin} + \mathcal{G}_{rot}	0.024 ± 0.003	1.104 ± 0.114	0.186 ± 0.073
\mathcal{G}^*_{nonlin} + \mathcal{G}^*_{rot}	$\textbf{0.035} \pm \textbf{0.013}$	1.181 ± 0.181	0.272 ± 0.122

6.2 Does latent PDE mapping improve geometric generalizability in 3D?

The results show that all PINNs can generalize to both the internal and external families when tested on rotations around the x-axis and on shearing along the yz-plane (\mathcal{H}_{rot}^x , \mathcal{H}_{rot}^{x*} , \mathcal{H}_{shear}^{yz} and $\mathcal{H}_{shear}^{yz*}$; Table 3). Beyond these settings, LPM-PINN and Affine-PINN generalize well to the remaining shearing directions and expansion families, whereas Basic-PINN struggles to make accurate predictions on the corresponding external families (Figure 6 in Appendix E.2). Table 3 further shows that LPM-PINN is the only PINN capable of handling rotations around the y- and z-axes. In these cases, both Affine-PINN and Basic-PINN produce entirely inaccurate predictions on the external families, as illustrated in Figure 3.

Table 3: Mean relative L_2 FEM-PINN discrepancy \pm std evaluated over the internal (\mathcal{H}_k^p) and external (\mathcal{H}_k^{p*}) test geometries from the geometry families in 3D.

	LPM-PINN	Affine-PINN	Basic-PINN
\mathcal{H}_{exp}	0.015 ± 0.001	0.015 ± 0.002	0.047 ± 0.019
\mathcal{H}^*_{exp}	$\textbf{0.050} \pm \textbf{0.017}$	0.082 ± 0.025	0.166 ± 0.044
$\mathcal{H}^{\omega g}$	$\textbf{0.020} \pm \textbf{0.006}$	0.023 ± 0.004	0.083 ± 0.027
$\mathcal{H}_{shear}^{shear}$	0.077 ± 0.030	$\textbf{0.075} \pm \textbf{0.020}$	0.212 ± 0.049
\mathcal{H}^{xz}_{shear}	0.020 ± 0.005	0.024 ± 0.004	0.078 ± 0.025
$\mathcal{H}_{shear}^{xz*}$	0.072 ± 0.029	$\textbf{0.068} \pm \textbf{0.017}$	0.209 ± 0.049
\mathcal{H}_{shear}^{yz}	0.015 ± 0.002	0.014 ± 0.001	0.016 ± 0.000
$\mathcal{H}_{shear}^{yz*}$	0.018 ± 0.005	0.017 ± 0.003	$\textbf{0.016} \pm \textbf{0.001}$
\mathcal{H}^{x}_{rot}	0.016 ± 0.004	0.021 ± 0.011	0.015 ± 0.001
\mathcal{H}_{rot}^{x*}	0.070 ± 0.034	0.073 ± 0.035	$\textbf{0.020} \pm \textbf{0.004}$
\mathcal{H}^y_{rot}	$\textbf{0.014} \pm \textbf{0.001}$	2.014 ± 0.188	0.234 ± 0.057
\mathcal{H}_{rot}^{y*}	$\textbf{0.036} \pm \textbf{0.023}$	1.212 ± 0.134	0.369 ± 0.094
$\overline{\mathcal{H}^z_{rot}}$	$\textbf{0.012} \pm \textbf{0.000}$	0.033 ± 0.006	0.224 ± 0.050
\mathcal{H}_{rot}^{z*}	$\textbf{0.014} \pm \textbf{0.002}$	0.402 ± 0.182	0.382 ± 0.074

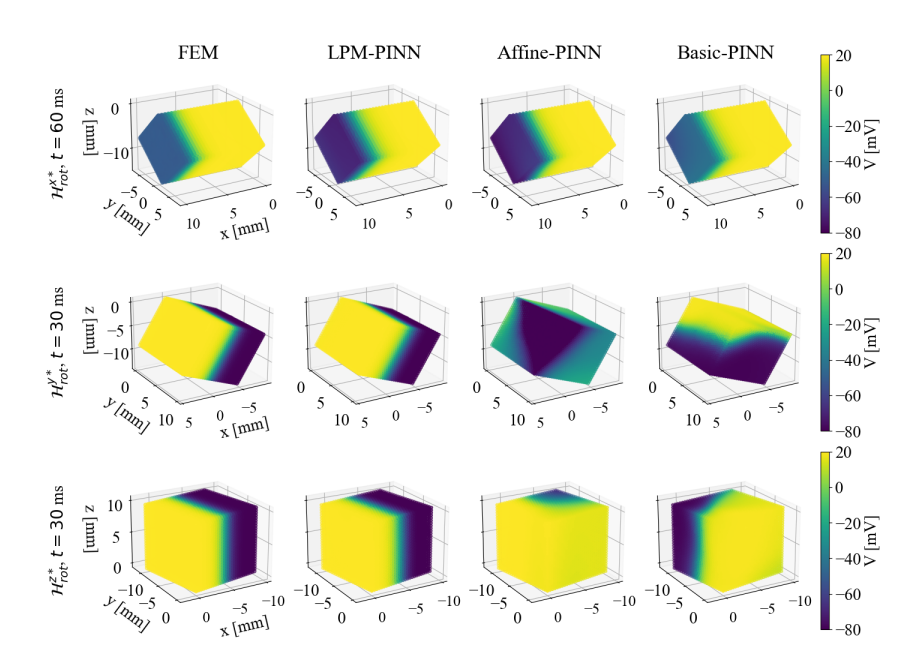


Figure 3: Snapshots of predicted transmembrane voltages (V). Each row corresponds to a geometry taken from the presented external family $(\mathcal{H}^{x*}_{rot}, \mathcal{H}^{y*}_{rot}, \mathcal{H}^{z*}_{rot})$ at a given time point. The left column shows the FEM ground truth approximation.

6.3 HOW LARGE ARE THE MISSING BOUNDARY SHAPE GRADIENTS WHEN LATENT PDE MAPPING IS NOT USED?

Figure 4 shows that the omitted boundary information (equation 11) in the shape gradients is large across all 2D cases (see Appendix F for computational details). For every family shown in Figure 4, the missing boundary information (blue) exceeds the shape gradient used in the Affine-PINN (orange). The magnitude of this missing information depends on the boundary movement when making changes to s (Figure 9a in Appendix F): the family with the smallest gap in Figure 4 also exhibits the smallest boundary change in Figure 9a. A similar trend appears in 3D, where shearing families show the lowest boundary changes (Figure 9b, Appendix F) and correspondingly small missing information (Figure 7, Appendix E.2), while expansion and rotational families exhibit larger

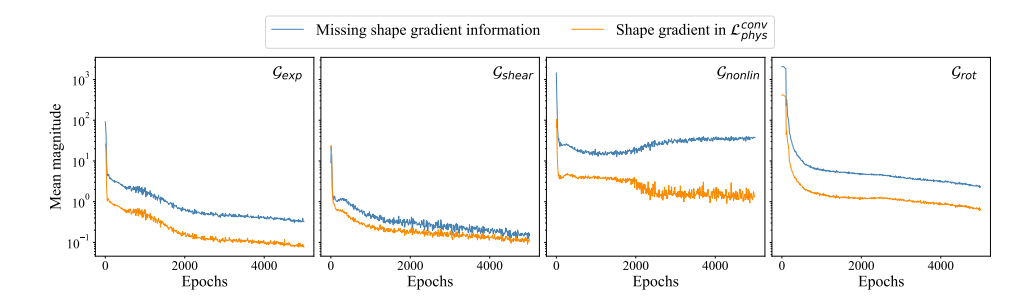


Figure 4: Numerical approximations of the missing shape gradients at the boundary and shape gradients used in $\mathcal{L}_{phys}^{conv}$ when training the Affine-PINN. The figure shows the mean magnitude across training geometries in \mathcal{G}_{exp} , \mathcal{G}_{shear} , \mathcal{G}_{nonlin} , and \mathcal{G}_{rot} .

boundary changes (Figure 9b, Appendix F) and larger omissions (Figure 8, Appendix E.2). These findings indicate that the missing boundary shape gradients are of substantial sizes when latent PDE mapping is not applied, leading to suboptimal learning.

7 DISCUSSION

This work presents *latent PDE mapping*, a novel technique for mapping geometry-specific PDEs to a shared latent PDE representation. Latent PDE mapping moves the shape dependence from the geometry into the PDE itself through the deformation gradient. This representation allows essential boundary information to be incorporated into the physics loss during training of PINNs (LPM-PINN).

The empirical results demonstrate that latent PDE mapping enhances generalization across diverse 2D and 3D geometries. In particular, the method is advantageous in scenarios where the training data comprises multiple geometric types (Table 2, Figure 5) or where boundary conditions undergo significant variation due to rotations (last row in Figure 2 and 3). In such settings, conventional PINNs that rely exclusively on shape descriptors exhibit reduced performance, while latent PDE mapping provides a more robust learning representation.

A central insight emerging from this study concerns the role of missing boundary shape gradients. In the absence of latent PDE mapping, the omitted boundary terms can be larger than the gradients actually employed for optimization (Figure 4). This omission can result in suboptimal PINNs that struggle to generalize beyond the training distribution.

The utility of latent PDE mapping depends on the overall boundary movement in the geometric families and on the PDE dynamics. Families with high boundary movements have a correspondingly higher missing boundary shape gradient when latent PDE mapping is not applied. Furthermore, latent PDE mapping improves learning and generalizability when geometric variability modifies the underlying PDE dynamics. In our case, the results show strong improvements when the initial activation site is moved substantially (last row in Figure 2 and 3).

Limitations and future work Our study has several limitations that open directions for future research. First, we relied on parameterized geometries, which may not always be available for more complex or realistic geometries encountered in real-world applications. Thus, extending latent PDE mapping to alternative shape representations is a critical future direction. One possibility is to employ principal component analysis modes as inputs to the PINN, rather than affine parameters, which has shown promise for representing cardiac geometries (Yin et al., 2024; Mauger et al., 2019). Second, the present study is restricted to simplified PDE dynamics, including planar waves and isotropic properties. Future work should evaluate latent PDE mapping under more challenging conditions, such as anisotropic properties and varying initial conditions. Finally, our validation of the advantage of latent PDE mapping was limited to rotation transformations and simple geometries. The effectiveness of latent PDE mapping in more complex geometries remains to be determined. This will be an essential next step for proving the applicability of latent PDE mapping in realistic industrial and medical scenarios.

REPRODUCIBILITY STATEMENT

Synthetic datasets can be created by following the description given in Section 4 and Appendix D with parameter ranges as presented in Table 4 in Appendix B.1 for 2D and Table 5 in Appendix B.2 for 3D. Implementation details regarding developed PINNs are presented in Section 5 and Appendix C, where the selected hyperparameters for each PINN are presented in Table 6. The source code and datasets used to reproduce results in Section 6 will be shared in the camera-ready submission, if accepted, to preserve anonymity during the double-blind review process.

REFERENCES

- Rubin R Aliev and Alexander V Panfilov. A simple two-variable model of cardiac excitation. *Chaos, Solitons & Fractals*, 7(3):293–301, 1996.
- Samuel Burbulla. Physics-informed neural networks for transformed geometries and manifolds. *arXiv preprint arXiv:2311.15940*, 2023.
- Francisco Sahli Costabal, Simone Pezzuto, and Paris Perdikaris. δ -pinns: physics-informed neural networks on complex geometries. *Engineering Applications of Artificial Intelligence*, 127: 107324, 2024.
- Salvatore Cuomo, Vincenzo Schiano Di Cola, Fabio Giampaolo, Gianluigi Rozza, Maziar Raissi, and Francesco Piccialli. Scientific machine learning through physics—informed neural networks: Where we are and what's next. *Journal of Scientific Computing*, 92(3):88, 2022.
- David Dalton, Dirk Husmeier, and Hao Gao. Physics-informed graph neural network emulation of soft-tissue mechanics. *Computer Methods in Applied Mechanics and Engineering*, 417:116351, 2023.
- Han Gao, Luning Sun, and Jian-Xun Wang. Phygeonet: Physics-informed geometry-adaptive convolutional neural networks for solving parameterized steady-state pdes on irregular domain. *Journal of Computational Physics*, 428:110079, 2021.
- Han Gao, Matthew J Zahr, and Jian-Xun Wang. Physics-informed graph neural galerkin networks: A unified framework for solving pde-governed forward and inverse problems. *Computer Methods in Applied Mechanics and Engineering*, 390:114502, 2022.
- Shinjan Ghosh, Julian Busch, Georgia Olympia Brikis, and Biswadip Dey. Geometry-aware pinns for turbulent flow prediction. *arXiv preprint arXiv:2412.01954*, 2024.
- Gerhard A. Holzaphel. *Nonlinear Solid Mechanics: A Continuum Approach for Engineering*. Wiley, 2000.
- George Em Karniadakis, Ioannis G Kevrekidis, Lu Lu, Paris Perdikaris, Sifan Wang, and Liu Yang. Physics-informed machine learning. *Nature Reviews Physics*, 3(6):422–440, 2021.
- Ali Kashefi and Tapan Mukerji. Physics-informed pointnet: A deep learning solver for steady-state incompressible flows and thermal fields on multiple sets of irregular geometries. *Journal of Computational Physics*, 468:111510, 2022.
- Charlène Mauger, Kathleen Gilbert, Aaron M Lee, Mihir M Sanghvi, Nay Aung, Kenneth Fung, Valentina Carapella, Stefan K Piechnik, Stefan Neubauer, Steffen E Petersen, et al. Right ventricular shape and function: cardiovascular magnetic resonance reference morphology and biventricular risk factor morphometrics in uk biobank. *Journal of Cardiovascular Magnetic Resonance*, 21(1):41, 2019.
- Francesco Mezzadri, Joshua Gasick, and Xiaoping Qian. A framework for physics-informed deep learning over freeform domains. *Computer-Aided Design*, 160:103520, 2023.
- openCARP consortium, Christoph Augustin, Patrick M. Boyle, Vincent Loechner, Raphaël Colin, Atoli Huppé, Matthias Gsell, Marie Houillon, Yung-Lin (Cary) Huang, Kristian Gregorius Hustad, Elias Karabelas, Axel Loewe, Lena Myklebust, Aurel Neic, Mark Nothstein, Gernot Plank, Anton Prassl, Jorge Sánchez, Gunnar Seemann, Tomas Stary, Arun Thangamani, Nico Tippmann,

- Tiago Trevisan Jost, Ed Vigmond, Eike Moritz Wülfers, and Moritz Linder. openCARP, 2024. URL https://git.opencarp.org/openCARP/openCARP.
 - Jiang-Zhou Peng, Nadine Aubry, Yu-Bai Li, Mei Mei, Zhi-Hua Chen, and Wei-Tao Wu. Physics-informed graph convolutional neural network for modeling geometry-adaptive steady-state natural convection. *International Journal of Heat and Mass Transfer*, 216:124593, 2023.
 - Gernot Plank*, Axel Loewe*, Aurel Neic*, Christoph Augustin, Yung-Lin (Cary) Huang, Matthias Gsell, Elias Karabelas, Mark Nothstein, Jorge Sánchez, Anton Prassl, Gunnar Seemann*, and Ed Vigmond*. The openCARP simulation environment for cardiac electrophysiology. *Computer Methods and Programs in Biomedicine*, 208:106223, 2021. doi: 10.1016/j.cmpb.2021.106223.
- Maziar Raissi, Paris Perdikaris, and George E Karniadakis. Physics-informed neural networks: A deep learning framework for solving forward and inverse problems involving nonlinear partial differential equations. *Journal of Computational physics*, 378:686–707, 2019.
- Francesco Regazzoni, Stefano Pagani, and Alfio Quarteroni. Universal solution manifold networks (usm-nets): non-intrusive mesh-free surrogate models for problems in variable domains. *Journal of Biomechanical Engineering*, 144(12):121004, 2022.
- Yubiao Sun, Ushnish Sengupta, and Matthew Juniper. Physics-informed deep learning for simultaneous surrogate modeling and pde-constrained optimization of an airfoil geometry. *Computer Methods in Applied Mechanics and Engineering*, 411:116042, 2023.
- Sifan Wang, Shyam Sankaran, Hanwen Wang, and Paris Perdikaris. An expert's guide to training physics-informed neural networks. *arXiv preprint arXiv:2308.08468*, 2023.
- Tobias Würth, Niklas Freymuth, Clemens Zimmerling, Gerhard Neumann, and Luise Kärger. Physics-informed meshgraphnets (pi-mgns): Neural finite element solvers for non-stationary and nonlinear simulations on arbitrary meshes. Computer Methods in Applied Mechanics and Engineering, 429:117102, 2024.
- Minglang Yin, Nicolas Charon, Ryan Brody, Lu Lu, Natalia Trayanova, and Mauro Maggioni. A scalable framework for learning the geometry-dependent solution operators of partial differential equations. *Nature Computational Science*, 4(12):928–940, 2024.
- Weiheng Zhong and Hadi Meidani. Physics-informed geometry-aware neural operator. *Computer Methods in Applied Mechanics and Engineering*, 434:117540, 2025.

A DERIVATION OF LATENT PDE MAPPING APPLIED TO THE ALIEV-PANFILOV PDE

In the following section, we give a detailed derivation of how the Aliev-Panfilov PDE in equation 7 is mapped from a physical geometry $\Omega(s)$ to a latent geometry Ω_0 . For convenience, we restate the equations over $\Omega(s)$ here as

$$\begin{cases} \frac{\partial V}{\partial \tau} = \nabla \cdot (\mathbf{D}\nabla V) - kV(V - a)(V - 1) - VW & \text{in } \Omega(s), \\ \frac{\partial W}{\partial \tau} = \left(\epsilon_0 + \frac{\mu_1 W}{V + \mu_2}\right) \left(-W - kV\left(V - a - 1\right)\right) & \text{in } \Omega(s), \\ \mathbf{D}\nabla V \cdot \boldsymbol{n} = 0 & \text{on } \partial\Omega(s). \end{cases}$$
(19)

The mapping is achieved by applying the deformation gradient $\mathbf{F}(\boldsymbol{X},t,s)$ and the deformation Jacobian $J(\boldsymbol{X},t,s)$ to quantities in equation 19, as well as performing a variable substitution $\boldsymbol{x}\to\boldsymbol{X}$ where $\boldsymbol{x}\in\Omega(s)$ and $\boldsymbol{X}\in\Omega_0$. The deformation gradient \mathbf{F} is given as

$$\mathbf{F}(X,t,s) = \mathbf{I} + \nabla U(X,t,s) \tag{20}$$

where U(X,t,s) = x(X,t,s) - X, while the deformation Jacobian is given as $J(X,t,s) = \det(\mathbf{F})$.

We start by introducing how quantities in equation 19 are mapped when applying principles from nonlinear solid mechanics (Holzaphel, 2000). Quantities that do not involve any divergences or gradients are mapped directly through a volume change defined as

$$dv = JdV (21)$$

where dv and dV are infinitesimally small volume elements in $\Omega(s)$ and Ω_0 , respectively. Gradients of a scalar field ϕ are mapped as

$$\nabla \phi(\boldsymbol{x}, t) = \mathbf{F}^{-T} \nabla \phi(\boldsymbol{X}, t) \tag{22}$$

which is obtained by applying the chain rule to $\nabla \phi(x,t)$. Finally, Nanson's formula is used to map vector elements from $\Omega(s)$ to Ω_0 . The formula yields

$$ds \mathbf{n} = J \mathbf{F}^{-T} dS \mathbf{N} \tag{23}$$

where dsn and dSN give the vector elements of infinitesimally small surface areas defined on $\Omega(s)$ and Ω_0 .

Next, we rewrite the divergence term in equation 19 in integral form as

$$\int_{\Omega(s)} \nabla \cdot (\mathbf{D} \nabla V) \mathrm{d}\Omega$$

By applying Gauss's divergence theorem, we have that

$$\int_{\Omega(s)} \nabla \cdot (\mathbf{D} \nabla V) d\Omega = \int_{\partial \Omega(s)} \mathbf{D} \nabla V \cdot ds \mathbf{n}$$
 (24)

where $\partial\Omega(s)$ is the surface of $\Omega(s)$ and n is the vector normal to the surface. We utilize the relationship of gradients in equation 22 and Nanson's formula in equation 23, such that the divergence term in equation 24 can be expressed over Ω_0 as

$$\int_{\partial\Omega(s)} \mathbf{D}\nabla V \cdot ds \boldsymbol{n} = \int_{\partial\Omega_0} \mathbf{D}\mathbf{F}^{-T} \nabla V \cdot J\mathbf{F}^{-T} dS \boldsymbol{N}$$
 (25)

In the 2D case, we have that

$$\mathbf{D} \in \mathbb{R}^{2x2}, \qquad \mathbf{F} \in \mathbb{R}^{2x2}, \qquad \nabla V \in \mathbb{R}^{2x1}.$$

Hence, by assuming that **F** is invertible, the terms in equation 25 can be reorganized as

$$\int_{\partial\Omega(s)} \mathbf{D}\nabla V \cdot ds \mathbf{n} = \int_{\partial\Omega_0} J \mathbf{F}^{-1} \mathbf{D} \mathbf{F}^{-T} \nabla V \cdot dS \mathbf{N}$$
 (26)

Finally, by applying Gauss's divergence theorem again, the divergence term in $\Omega(s)$ and Ω_0 can be expressed as

$$\int_{\Omega(s)} \nabla \cdot (\mathbf{D} \nabla V) d\Omega = \int_{\Omega_0} \nabla \cdot \left(J \mathbf{F}^{-1} \mathbf{D} \mathbf{F}^{-T} \nabla V \right) d\Omega_0$$
 (27)

By following the same procedure, the boundary condition in equation 19 can be rewritten as

$$\int_{\Omega(s)} (\mathbf{D}\nabla V \cdot \boldsymbol{n}) d\Omega = \int_{\Omega_0} (J\mathbf{F}^{-1}\mathbf{D}\mathbf{F}^{-T}\nabla V \cdot \boldsymbol{N}) d\Omega_0$$
 (28)

The remaining parts of equation 19 do not include any divergences or gradients, and are mapped directly through a volume change as defined in equation 21. Consequently, equation 19 can be expressed over Ω_0 as

$$\begin{cases} \frac{\partial}{\partial \tau}(JV) = \nabla \cdot (J\mathbf{F}^{-1}\mathbf{D}\mathbf{F}^{-T}\nabla V) - JkV(V-a)(V-1) - JVW & \text{in } \Omega_0, \\ \frac{\partial}{\partial \tau}(JW) = J\left(\epsilon_0 + \frac{\mu_1 W}{V+\mu_2}\right)\left(-W - kV\left(V-a-1\right)\right) & \text{in } \Omega_0, \\ J\mathbf{F}^{-1}\mathbf{D}\mathbf{F}^{-T}\nabla V \cdot \mathbf{N} = 0 & \text{on } \partial\Omega_0, \end{cases} \tag{29}$$

For time-independent mappings, we finally arrive at

$$\begin{cases} \frac{\partial V}{\partial \tau} = \frac{1}{J} \nabla \cdot (J \mathbf{F}^{-1} \mathbf{D} \mathbf{F}^{-T} \nabla V) - kV(V - a)(V - 1) - VW & \text{in } \Omega_0, \\ \frac{\partial W}{\partial \tau} = \left(\epsilon_0 + \frac{\mu_1 W}{V + \mu_2} \right) (-W - kV(V - a - 1)) & \text{in } \Omega_0, \\ J \mathbf{F}^{-1} \mathbf{D} \mathbf{F}^{-T} \nabla V \cdot \mathbf{N} = 0 & \text{on } \partial \Omega_0, \end{cases}$$
(30)

B ADDITIONAL DETAILS ON DATASET GENERATION

B.1 2D GEOMETRIES

Table 4 presents the data ranges used when creating the first three internal (\mathcal{G}_k) and external (\mathcal{G}_k^*) families in 2D. Additionally, the rotational family (\mathcal{G}_{rot}) and (\mathcal{G}_{rot}) was created by defining \mathbf{A} as a rotational matrix

$$\mathcal{G}_{rot} \text{ and } \mathcal{G}_{rot}^* : \quad \mathbf{A} = \begin{bmatrix} \cos(\theta) & -\sin(\theta) \\ \sin(\theta) & \cos(\theta) \end{bmatrix}$$
 (31)

with $\theta \in [-\frac{\pi}{2}, \frac{\pi}{2}]$ for \mathcal{G}_{rot} and $\theta \notin [-\frac{\pi}{2}, \frac{\pi}{2}]$ for \mathcal{G}^*_{rot} . All values were sampled uniformly from the given ranges.

Table 4: Parameter ranges for the first three internal (\mathcal{G}_k) and external (\mathcal{G}_k^*) families in 2D. Values were sampled uniformly from the given ranges.

	a_1, a_4	a_{2}, a_{3}	m_1, m_4
$\overline{\mathcal{G}_{exp}}$	[1.0, 1.4]	0.0	0.0
\mathcal{G}_{exp}^*	[1.4, 1.8]	0.0	0.0
\mathcal{G}_{shear}	1.0	[-0.2, 0.2]	0.0
\mathcal{G}^*_{shear}	1.0	$[-0.5, -0.2] \cup [0.2, 0.5]$	0.0
\mathcal{G}_{nonlin}	1.0	0.0	[-0.015, 0.015]
\mathcal{G}^*_{nonlin}	1.0	0.0	$[-0.025, -0.015] \cup [0.015, 0.025]$

B.2 3D GEOMETRIES

In 3D, we constructed seven families by applying linear affine transformations to a $10 \times 10 \times 10$ mm cube. The linear transformations were defined as

$$x = AX \tag{32}$$

Table 5: Parameter ranges for the internal (\mathcal{H}_k) and external (\mathcal{H}_k^*) expansion/shearing families in 3D. All values were sampled uniformly from the given ranges.

	a_1, a_5, a_9	a_2, a_4	a_3, a_7	a_6, a_8
\mathcal{H}_{exp}	[1.0, 1.4]	0.0	0.0	0.0
\mathcal{H}^*_{exp}	[1.4, 1.8]	0.0	0.0	0.0
\mathcal{H}_{shear}^{xy}	1.0	[-0.2, 0.2]	0.0	0.0
\mathcal{H}_{shear}^{xy} $\mathcal{H}_{shear}^{xy*}$	1.0	$[-0.5, -0.2] \cup [0.5, 0.2]$	0.0	0.0
\mathcal{H}^{xz}_{shear}	1.0	0.0	[-0.2, 0.2]	0.0
$\mathcal{H}_{shear}^{xz*}$	1.0	0.0	$[-0.5, -0.2] \cup [0.5, 0.2]$	0.0
\mathcal{H}^{yz}_{shear}	1.0	0.0	0.0	[-0.2, 0.2]
$\mathcal{H}^{yz}_{\substack{shear \ \mathcal{H}^{yz*} \ shear}}$	1.0	0.0	0.0	$[-0.5, -0.2] \cup [0.5, 0.2]$

with

$$\mathbf{A} = \begin{bmatrix} a_1 & a_2 & a_3 \\ a_4 & a_5 & a_6 \\ a_7 & a_8 & a_9 \end{bmatrix} . \tag{33}$$

Similarly to the 2D scenario, each family was constructed using a distinct deformation type: expansion (\mathcal{H}_{exp}) , shearing (\mathcal{H}_{shear}) , and rotation (\mathcal{H}_{rot}) . The parameter ranges used for the expansion and shearing families are presented in Table 5. Additionally, for the rotational families, \boldsymbol{A} was defined as

$$\mathcal{H}_{rot}^{x} \text{ and } \mathcal{H}_{rot}^{x*}: \quad \boldsymbol{A} = \begin{bmatrix} 1.0 & 0.0 & 0.0 \\ 0.0 & \cos(\theta) & -\sin(\theta) \\ 0.0 & \sin(\theta) & \cos(\theta) \end{bmatrix},$$

$$\mathcal{H}_{rot}^{y} \text{ and } \mathcal{H}_{rot}^{y*}: \quad \boldsymbol{A} = \begin{bmatrix} \cos(\theta) & 0.0 & \sin(\theta) \\ 0.0 & 1.0 & 0.0 \\ -\sin(\theta) & 0.0 & \cos(\theta) \end{bmatrix},$$

$$\mathcal{H}^{z}_{rot} \text{ and } \mathcal{H}^{z*}_{rot}: \quad \boldsymbol{A} = \begin{bmatrix} \cos(\theta) & -\sin(\theta) & 0.0 \\ \sin(\theta) & \cos(\theta) & 0.0 \\ 0.0 & 0.0 & 1.0 \end{bmatrix},$$

with $\theta \in [-\frac{\pi}{2}, \frac{\pi}{2}]$ for internal families and $\theta \notin [-\frac{\pi}{2}, \frac{\pi}{2}]$ for external families. All values were sampled uniformly from the given ranges.

C HYPERPARAMETERS AND IMPLEMENTATION DETAILS

Table 6 presents the hyperparameters used in each PINN. The PINNs were implemented with *Py-Torch*, and experiments were run on NVIDIA HGX H200 GPUs.

D ADDITIONAL DETAILS ON SYNTHETIC DATA GENERATION

We generated the synthetic data using *openCARP* (Plank* et al., 2021; openCARP consortium et al., 2024) with parameters as listed in Table 7. Before running the simulation, we meshed the physical geometry using triangular elements in 2D and tetrahedral elements in 3D. The maximum element size was set to 0.05 and 0.4 in 2D and 3D, respectively.

E SUPPLEMENTARY RESULTS

E.1 2D RESULTS

Figure 5 illustrates snapshots of predicted transmembrane potential (V) for selected geometries when the PINNs were trained on a combination of two families.

Table 6: Overview of PINN configurations.

		LPM-PINN	Affine-PINN	Basic-PINN
Innut dim	2D	9	9	3
Input dim	3D	16	16	4
Hidden dim		25	25	25
Output dim		2	2	2
Hidden layers		10	10	10
Epochs		5000	5000	5000
Batch size		264	264	264
Optimizer		Adam	Adam	Adam
I coming note	< 100 epochs	10^{-3}	10^{-3}	10^{-3}
Learning rate	> 100 epochs	10^{-4}	10^{-4}	10^{-4}
Activation		tanh	tanh	tanh
\mathcal{N}_{data}		14	14	14
\mathcal{N}_{phys} (resampled)		700	700	700
\mathcal{N}_{bc} (resampled)		80	80	80
\mathcal{N}_{ic} (resampled)		30	30	30

Table 7: Parameter values used to create synthetic data.

Parameter	Description	Value
C_m	membrane capacitance	$1\mathrm{\mu Fcm}^{-2}$
β	surface area to volume ratio	$0.14 \mu { m m}^{-1}$
f_x, f_y, f_z	fiber orientation	1, 0, 0
Δt	time resolution	$1\mathrm{ms}$
I_{app}	applied stimuli	$5000 \mu \mathrm{Acm}^{-2}$ for $0.2 \mathrm{ms}$ (planar wave)
g_{il}	intracellular longitudinal conductivity	$0.2 {\rm Sm}^{-1}$
g_{it}	intracellular transversal conductivity	$0.2 {\rm Sm}^{-1}$
g_{in}	intracellular normal conductivity	$0.2 {\rm Sm}^{-1}$
g_{el}	extracellular longitudinal conductivity	$1.0{\rm Sm}^{-1}$
g_{et}	extracellular transversal conductivity	$1.0{\rm Sm}^{-1}$
g_{en}	extracellular normal conductivity	$1.0{\rm Sm}^{-1}$

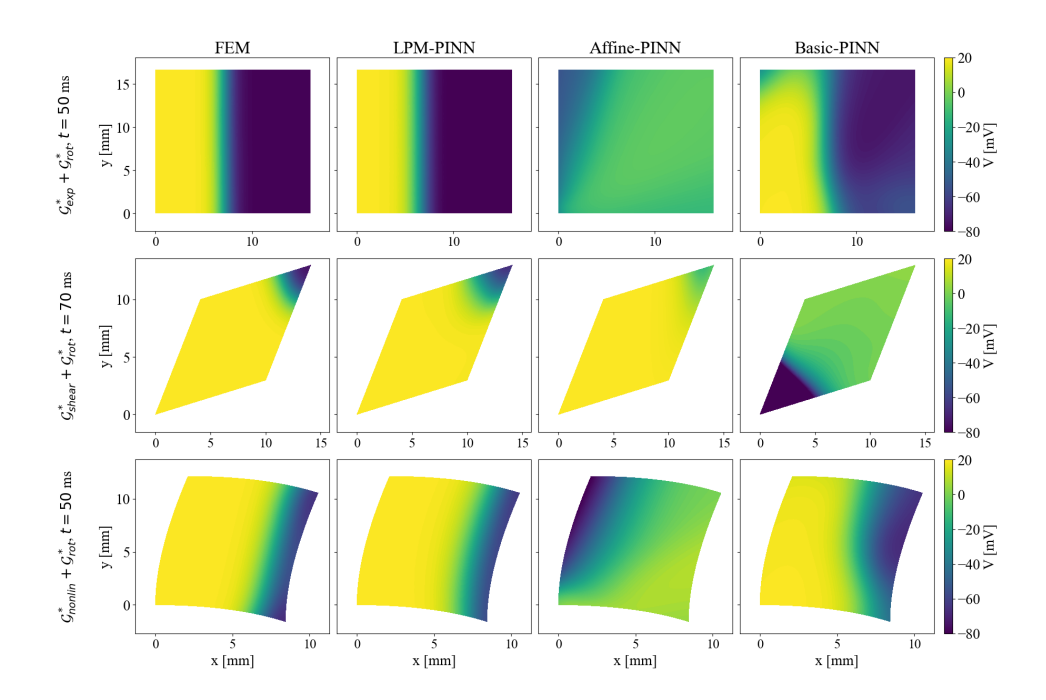


Figure 5: Snapshot of predicted transmembrane voltages (V) for a geometry taken from \mathcal{G}^*_{exp} , \mathcal{G}^*_{shear} , and \mathcal{G}^*_{nonlin} at the given time point. The PINNs were trained on a combination of geometries from the given families. The left column shows the FEM ground truth approximation.

E.2 3D RESULTS

Figure 6 visualizes snapshots of the predicted transmembrane potential (V) for selected geometries, while Figures 7 and 8 show the numerical approximation of missing shape gradients at the boundaries for expansion, shearing, and rotational families.

F COMPUTATIONAL DETAILS OF MISSING BOUNDARY INFORMATION

In the following section, we present details on how equation 11 was discretized and numerically approximated. For convenience, we restate the equation here as

$$\frac{\partial \mathcal{L}_{phys}}{\partial s} = \int_{\Omega(s)} \frac{\partial}{\partial s} \mathcal{R}(\boldsymbol{x}, t, u, s)^2 d\Omega + \int_{\partial \Omega(s)} \mathcal{R}(\boldsymbol{x}, t, u, s)^2 \frac{\partial \boldsymbol{x}}{\partial s} \cdot \boldsymbol{n} dS$$
(34)

and define

$$I(s) \equiv \int_{\Omega(s)} \frac{\partial}{\partial s} \mathcal{R}(\boldsymbol{x}, t, u, s)^2 d\Omega$$
 (35)

$$B(s) \equiv \int_{\partial\Omega(s)} \mathcal{R}(\boldsymbol{x}, t, u, s)^2 \frac{\partial \boldsymbol{x}}{\partial s} \cdot \boldsymbol{n} dS$$
 (36)

such that

$$\frac{\partial \mathcal{L}_{phys}}{\partial s} = I(s) + B(s). \tag{37}$$

Next, we discretize the terms and make a numerical approximation using Monte Carlo for integrals and central finite differences for derivatives. We assume that the spatial positions are uniformly distributed and normalize with respect to the area/boundary, such that

$$I(s_k) \approx \frac{1}{N_I(s)} \sum_{i}^{N_I(s)} \sum_{j}^{T} \frac{\mathcal{R}(x_i, t_j, u_{ij}, s_k + \Delta s)^2 - \mathcal{R}(x_i, t_j, u_{ij}, s_k - \Delta s)^2}{2\Delta s}$$
(38)

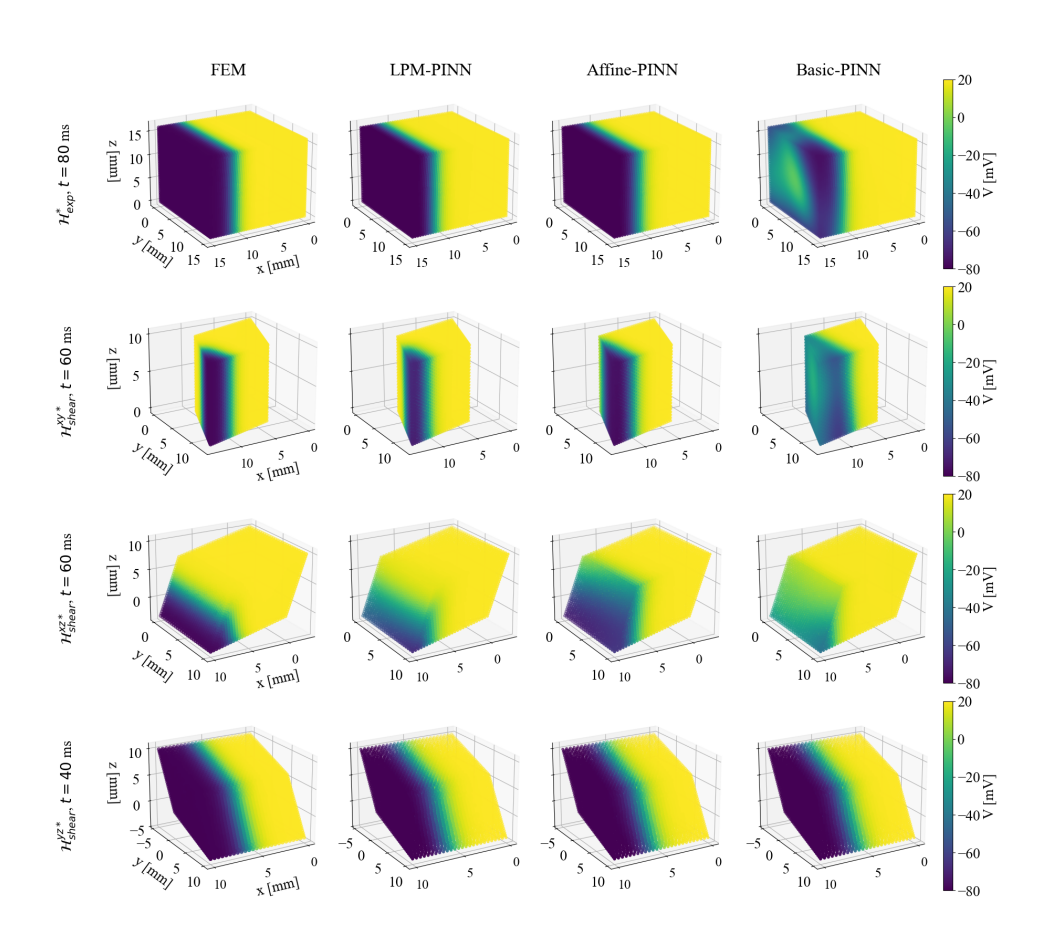


Figure 6: Snapshots of predicted transmembrane voltages (V). Each row corresponds to a geometry taken from the presented external family $(\mathcal{H}^*_{exp}, \mathcal{H}^{xy*}_{shear}, \mathcal{H}^{xz*}_{shear}, \mathcal{H}^{yz*}_{shear})$ at a given time point. The left column shows the FEM ground truth approximation.

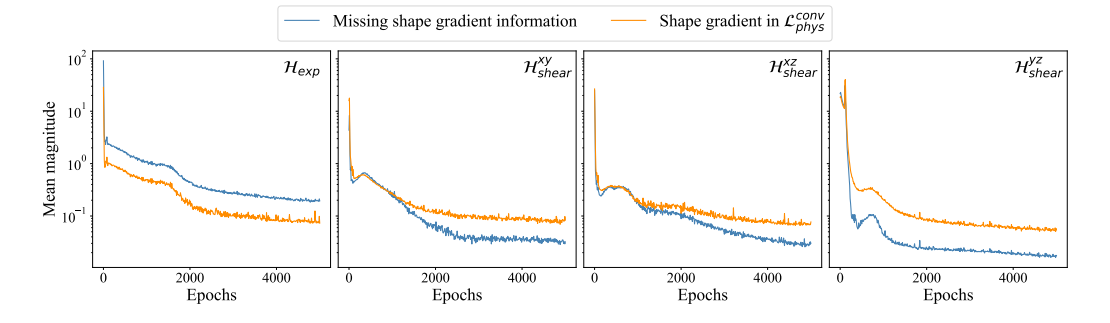


Figure 7: Numerical approximations of the missing shape gradients at the boundary and shape gradients used in $\mathcal{L}_{phys}^{conv}$ when training the Affine-PINN. The figure shows the mean magnitude across training geometries in \mathcal{H}_{exp} , \mathcal{H}_{shear}^{xy} , \mathcal{H}_{shear}^{xz} , and \mathcal{H}_{shear}^{yz} .

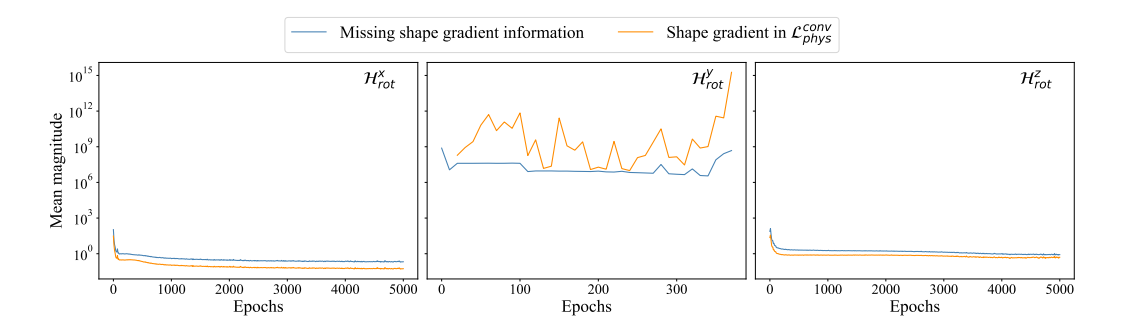


Figure 8: Numerical approximations of the missing shape gradients at the boundary and shape gradients used in $\mathcal{L}_{phys}^{conv}$ when training the Affine-PINN. The figure shows the mean magnitude across training geometries in \mathcal{H}_{rot}^x , \mathcal{H}_{rot}^y , and \mathcal{H}_{rot}^z .

and

$$B(s_k) \approx \frac{1}{N_B(s)} \sum_{i}^{N_B(s)} \sum_{j}^{\mathcal{T}} \mathcal{R}(\boldsymbol{x}_i, t_j, u_{ij}, s_k)^2 \underbrace{\frac{\boldsymbol{x}_i(s_k + \Delta s) - \boldsymbol{x}_i(s_k - \Delta s)}{2\Delta s} \cdot \boldsymbol{n}_i(s)}_{\text{boundary movement}} \cdot \boldsymbol{n}_i(s)$$
(39)

where s_k is the k-th value in a set of shape parameters given as $s = \{s_1, s_2, ..., s_K\}$. Moreover, $N_I(s)$ and $N_B(s)$ gives the number of spatial positions used to evaluate the two terms and \mathcal{T} is the total number of time steps. Thus, our discretized version for the k-th shape value is given as

$$\frac{\Delta \mathcal{L}_{phys}}{\Delta s_k} = I(s_k) + B(s_k) \tag{40}$$

The magnitude of the overall change for the shape parameters $(\frac{\Delta \mathcal{L}_{phys}}{\Delta s})$ was computed by applying the L_2 norm to equation 40. Finally, we computed $\frac{\Delta \mathcal{L}_{phys}}{\Delta s}$ for each geometry in a family, and represented the numerical approximation of I and B as the mean across the given geometries. Here, I represents the numerical computation of $\mathcal{L}_{phys}^{conv}$ and B represents the missing boundary information when latent PDE mapping is not applied (see Figures 4, 7, and 8). We used $\Delta s = 10^{-6}$ in all computations.

F.1 BOUNDARY MOVEMENTS

The magnitude of the numerically approximated boundary movements when making small changes to the shape parameters s for each family in 2D and 3D are presented in Figure 9a and 9b, respectively. The boundary movements were approximated by applying central finite differences, as shown in equation 39, yielding

$$\frac{\Delta \boldsymbol{x}}{\Delta s_k} = \frac{1}{N_B(s)} \sum_{i}^{N_B(s)} \frac{\boldsymbol{x}_i(s_k + \Delta s) - \boldsymbol{x}_i(s_k - \Delta s)}{2\Delta s} \cdot \boldsymbol{n}_i(s)$$
(41)

where $N_B(s)$ gives the number of boundary points. Again, the overall magnitude of the boundary movement was computed using the L_2 norm and mean across the given geometries with $\Delta s = 10^{-6}$.

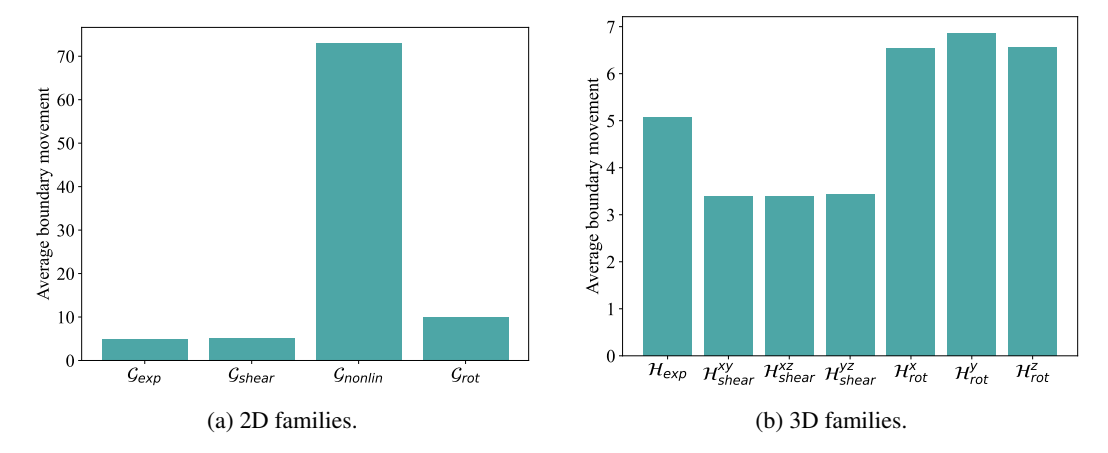


Figure 9: Numerical approximations of boundary movements when making small changes to the shape parameters s for each family in 2D and 3D.